applied sciences

MDPI

Article

Numerical Study on the Sagging Damage of the Simplified Hull Girder Subjected to Underwater Explosion Bubble

Yuxiang Gong [1], Wenpeng Zhang [1,*], Zhipeng Du [1,2] and Yinghao Zhu [1]

[1] School of Mechanical Engineering, Shenyang University of Technology, Shenyang 110000, China
[2] Naval Research Academy, Beijing 100161, China
* Correspondence: zwp16@sut.edu.cn; Tel.: +86-15110022328

Abstract: The pulsation of the bubbles resulting from underwater explosions can lead to severe damage to the structure of the ship's hull, and even to its sinking. To study the damage mechanism of a simplified hull girder (SHG) subjected to near-field underwater explosion bubble, the Coupled Eulerian–Lagrangian (CEL) method based on verifications of the calculation accuracy was used to simulate 11 SHG structures. The sagging bend mechanism of SHGs was analyzed from the perspective of plastic hinge lines. Moreover, the length formula of the potential bend zone was studied through the assumed plastic hinge lines. The influence of transverse bulkheads on bending mode and total longitudinal strength was investigated. The results show that SHGs' sagging damage is composed of regular plastic hinge lines, mainly depending on side plates' folding—W-shaped in this paper. When facing the near-field underwater explosion bubble, the distant transverse bulkheads influence the total longitudinal strength and do not always play a positive role.

Keywords: simplified hull girder; underwater explosion; explosion bubble; sagging damage

check for updates

Citation: Gong, Y.; Zhang, W.; Du, Z.; Zhu, Y. Numerical Study on the Sagging Damage of the Simplified Hull Girder Subjected to Underwater Explosion Bubble. *Appl. Sci.* **2023**, *13*, 2318. https://doi.org/10.3390/app13042318

Academic Editors: Jeong-Hwan Kim and Jeong-Hyeon Kim

Received: 8 January 2023
Revised: 6 February 2023
Accepted: 7 February 2023
Published: 10 February 2023

Copyright: © 2023 by the authors. Licensee MDPI, Basel, Switzerland. This article is an open access article distributed under the terms and conditions of the Creative Commons Attribution (CC BY) license (https://creativecommons.org/licenses/by/4.0/).

1. Introduction

Underwater explosions are one of the main threats to warships in the ocean [1–3]. Unlike the air blast, the bubbles formed by the underwater explosion products may cause fatal damage to ships. Therefore, researchers have been continuously studying the explosion bubbles and the structural damage response. At first, most of these studies were focused on the far field. Widely used far-field bubble load models were given by Zamyshlyayev [4], Vernon [5], and Geers [6], respectively. However, with the progress of weapon technology, there are more and more scenes of ships being attacked by near-field underwater explosions. When the distance between the explosive and the structure becomes closer, the bubble shows some new complex phenomena in its evolution, and damage to the structure is more likely to occur, so research conclusions regarding the far field are difficult to fully apply.

To further explore the near-field explosion bubbles and the damage rules caused by them, scholars have used experimental and simulation methods to carry out their studies in recent years. Some scholars have focused on the load law of explosive bubbles near boundaries. Through a recently developed computational framework that couples a finite volume compressible fluid dynamics solver with a finite element structural dynamics solver, Ma et al. [7] found three different modes of bubble collapse. By using the CEL method to study the evolution process of an underwater explosion bubble under boundary conditions near the water surface, near a submerged cylinder and the rigid bottom, Gannon [8] evaluated the CEL method's ability to predict underwater explosion load near the interface. Similarly, Javier et al. [9] also applied the CEL method to study the interaction between the explosive bubble and the rigid wall. It can be seen that the CEL method has considerable applicability in research on near-field underwater explosions.

Some researchers focused on the structural responses in the near-field underwater explosion situation. In terms of local damage, Ramajeyathilagam [10], Chung Kim Yuen [11],

and Suresh [12] conducted many close underwater explosion experiments on square plate structures. The research results provide a powerful criterion for predicting the local damage to ships. Considering the excellent energy absorption characteristics of sandwich structures, Schiffer [13], Zhang [14], and Gargano [15] studied these anti-impact performances under an underwater explosion load, providing a basis for the effective protection of offshore structures. In addition, Mohotti [16] and Liu [17] studied the effect of the covering layer on the anti-impact performance of the steel plate structures, analyzed the optimal parameters of the covering layer, and provided a new idea to improve the vitality of the ship.

To explore the overall damage rule of near-field underwater explosion bubbles to ships, the simplified hull girders (SHGs) with similar response characteristics to the real ship have become an important research object. In the paper by Zhang [18], the coupling effect of overall motion and local deformation on SHG was discussed through an experiment case. Likewise, Li et al. [19,20] conducted experimental studies on the overall damage characteristics of the same SHG at various load conditions. The results show that there are two main kinds of damage phenomena: hogging damage related to shock wave and sagging damage caused by bubble pulsation. Moreover, Wang et al. [21] used the three-dimensional boundary integral method to simulate the interaction between surface ships and near-field underwater explosion bubbles, finding that bubbles' negative pressure effect is an important reason for sagging damage. Gan et al. [22,23] twice analyzed the sagging damage mechanism of SHGs under various explosion cases, mainly using the CEL simulation method based on experimental verification. These studies show that when the shock wave of underwater explosives is not enough to cause severe damage, the subsequent bubble pulsation may lead to sinking. (The contents of the underwater explosion involved in the Introduction are summarized in Figure 1.) However, most of the current work regarding the sagging damage mechanism of SHGs is carried out using different loads on the same SHG. The similarities and differences in damage mode between different SHGs and the local damage pattern at the bend zone have yet to be fully discussed.

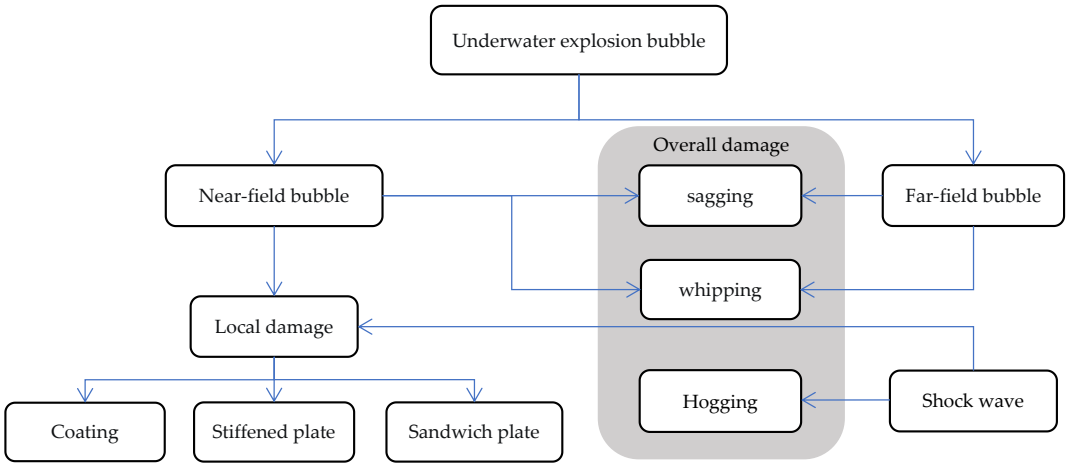


Figure 1. Underwater explosion ship damage summarized in the introduction.

In this paper, based on the verification of the model's calculation accuracy, the CEL Abaqus/explicit method is employed to simulate the response process of 11 different open SHGs subjected to near-field underwater explosions. The local creases pattern and plastic hinge lines mechanism at the bend zone are analyzed. Moreover, the formula for the length of the potential bend zone is given. Then, the effect of the transverse bulkheads on bend mode and total longitudinal strength is investigated. A new performance parameter, named the equivalent moment of inertia parameter, is constructed to evaluate the overall longitudinal bend strength of SHGs in cases of sagging damage under the near-field underwater explosion.

2. Numerical Method

2.1. The Coupled Eulerian–Lagrangian (CEL) Method

During near-field underwater explosion simulation, the traditional Lagrange and Euler grid algorithms have limitations. The Lagrange algorithm would like severe distortion in the elements. The Euler algorithm struggles to accurately capture the material boundary. Therefore, the coupled Euler–Lagrange (CEL) method is proposed to solve the above weaknesses. The CEL method combines the advantages of the two traditional grid algorithms, processing the structure and fluid separately, and carrying out the coupling calculation on the contact surface to better solve the complex fluid–structure coupling problem and large deformation problem. In calculation, the Lagrange method was adopted to solve the structure. The movement and deformation of the elements could be generated, along with the flow of materials. The governing equations can be expressed as [24]:

$$\begin{aligned} \frac{d\rho}{dt} + \rho\nabla \cdot v &= 0 \\ \rho\frac{dv}{dt} &= \nabla \cdot \sigma + \rho b \\ \rho\frac{de}{dt} &= \sigma : (\nabla \otimes v), \end{aligned} \tag{1}$$

where ρ, v, e, σ, and b are the density, velocity, specific internal energy, stress, and mass forces of the Lagrangian medium, respectively.

The fluid is solved by the Euler method. When a response occurs, the mesh is fixed without movement, and the material is transported among the elements. The governing equations can be written as follows [24]:

$$\begin{aligned} \frac{\partial\rho}{\partial t} + \nabla \cdot (\rho v) &= 0 \\ \frac{\partial\rho v}{\partial t} + \nabla \cdot (\rho v \otimes v) &= \nabla \cdot \sigma + \rho b \\ \frac{\partial e}{\partial t} + \nabla \cdot (ev) &= \sigma : (\nabla \otimes v), \end{aligned} \tag{2}$$

where ρ, v, e, σ, and b are the density, velocity, specific internal energy, stress, and mass forces of the Euler fluid medium, respectively. At the interface, the velocity on the Lagrangian boundary provides the constrained kinetic energy for the Euler calculation, and the Euler material's pressure provides the Lagrangian region's loading force. Lagrangian and Euler solvers interact through the coupling surface.

It should be noted that the CEL method requires high computational power support to simulate underwater explosions. Although Abaqus provides the setting of non-reflection boundaries, it can only reduce the influence of wave reflection to a certain extent. Therefore, a large Euler domain is still needed, and a high-accuracy mesh division is required around the explosive. When calculating the long analysis time of explosion bubbles, the problem of high calculation consumption becomes more prominent.

2.2. Material Models

Materials used in this paper include water, air, TNT, and Q235 steel. The us-Up equation of state was adopted to simulate water motion under explosion loads. The equation [25] is written as follows:

$$U_s = c_0 + sU_p, \tag{3}$$

where c_0 and s define the linear impact velocity U_s and particle velocity U_p, the density of water ρ_0 is 1000 kg/m^3, and the sound velocity in water c_0 is 1450 m/s.

The air is regarded as an ideal gas, with the expression [25]:

$$P + P_A = \rho R(\theta - \theta_Z), \tag{4}$$

where ρ is the air density, taken as 1.225 kg/m^3, the ambient pressure P_A is 101,325 Pa, R is the gas constant, θ is the current temperature, and θ_Z is absolute zero in temperature.

JWL equation of state, widely used in the field of explosion and impact, is used to describe TNT explosives. The expression [25] can be given as:

$$P = A\left(1 - \frac{\omega\rho}{R_1\rho_0}\right)e^{\left(-R_1\frac{\rho_0}{\rho}\right)} + B\left(1 - \frac{\omega\rho}{R_2\rho_0}\right)e^{\left(-R_2\frac{\rho_0}{\rho}\right)} + \omega\rho E_m, \quad (5)$$

where A, B, R_1, R_2, ω are material constants defined by the experimental results. ρ_0 is the explosive density, ρ is the detonation product density, E_m is the internal energy per unit mass of the explosive, and the specific values are listed in Table 1.

The structure material is Q235 steel with a density of 7850 kg/m^3, Young's modulus of 2.1×10^{11} Pa, and Poisson's ratio of 0.3. The plastic parameters [23], including strain rates, are given in Table 2.

Table 1. TNT explosive parameters.

ρ_0/(kg/m^3)	A (GPa)	B (GPa)	R_1	R_2	ω	E_m (J/kg)
1630	371.2	3.21	4.15	0.95	0.3	4.29×10^6

Table 2. Q235 steel material parameters.

Yield Stress/Pa	Plastic Strain	Strain Rate /(1/S)
2.35×10^8	0	0
3.75×10^8	0.3	0
5.17×10^8	0	100
8.25×10^8	0.3	100
8.51×10^8	0	5000
1.358×10^9	0.3	5000

3. Simulation Model

3.1. Simulation Arrangements

With reference to Gan's near-field underwater explosion SHG experiment [23], the simulation arrangements are shown in Figure 2. The draft depth of the structure was 0.08 m. The TNT explosive was located in the water directly below the center of the structure. To avoid the influence of Euler boundary reflection on bubble results, the Euler domain should be large enough. Referring to the simulation settings of similar cases in reference [23], the flow field size was modeled as 5 m × 5 m × 2.5 m (length, width, height, sequentially), while the water field was 1.9 m high and the air field was 0.6 m high. According to experience, the mesh within three times the bubble radius should be densified. Considering the size of the bubble radius, SHG structure, and SHG moving range, the mesh in the 1.7 m × 1.2 m × 2.5 m (length, width, height, sequentially) area around the explosive was the main focus. After the mesh sensitivity inspection, a model containing 2.9 million elements (the minimum mesh size is 0.01 m) was selected within the allowable range of computational power. The comparison results of the different meshes are shown in Figure 3. The hexahedral Euler elements were used for the flow field. S4R elements were used for structures. The Euler boundary setting was the same as the actual situation, with surrounding walls to prevent the medium from flowing out.

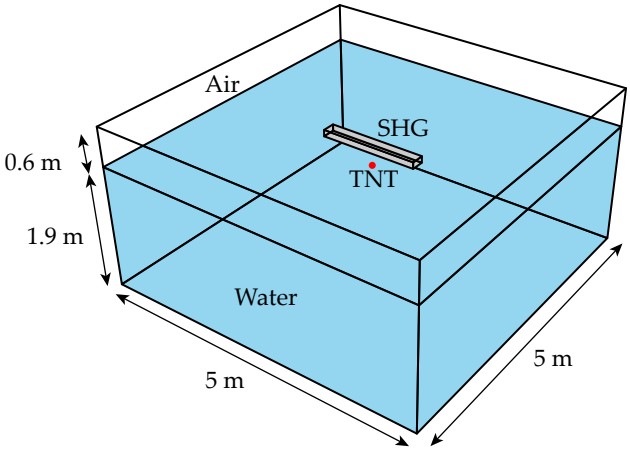


Figure 2. Arrangements diagram of underwater explosion simulation.

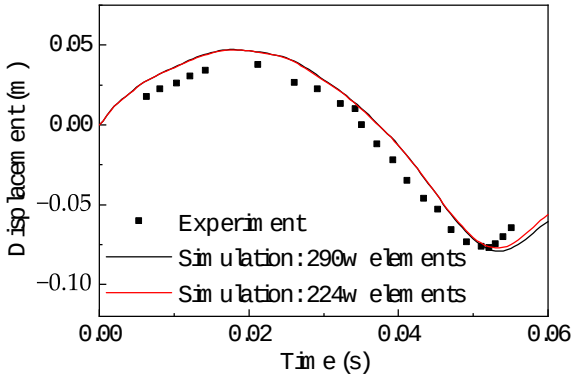


Figure 3. Displacement results of middle section.

3.2. Validation of Simulation Model

To investigate the validity of the calculation method and the established model, the SHG structure in Gan's experiment was calculated in this case [23]. The loading conditions were as follows: TNT mass was 0.01 kg, detonation distance from the explosive to SHG's bottom plate was 0.25 m (impact factor SF = 0.180). Figure 4 compares stress nephograms with experimental photos [23] at different times. In the legend, S. Mises means Mises stress, SNEG means the bottom surface of the shell element, and Avg: 75% is the software default nephogram average threshold. After the explosive was detonated, the free-floating SHG first produced the initial upward movement, with slight overall hogging deformation and stress concentration at the midship. Then, during the subsequent bubble evolution process, the upper part of the bubble gradually tended to be irregular due to the joint influence of the structure and the free liquid surface. At 20 ms, the bubble in the expansion stage continued to drive the SHG upward. However, mainly due to the inertial effect and material resilience, the structure recovered from the hogging bend to the horizontal state. Moreover, a W-shaped stress concentration appeared in the middle of the side plates, indicating a downward bend trend. Subsequently, under the action of the shrinkage bubble's low pressure, the structure moved downward. The middle part of the SHG bent down significantly, and the side plates appeared to be folded due to compression, causing overall sagging damage. At the later stage of shrinkage, the bubble broke into bubble swarms under the combined action of air, structure, and free liquid surface. At 55 ms, the SHG's sagging amplitude was restored to a certain extent because of the relief of the low-pressure bubble.

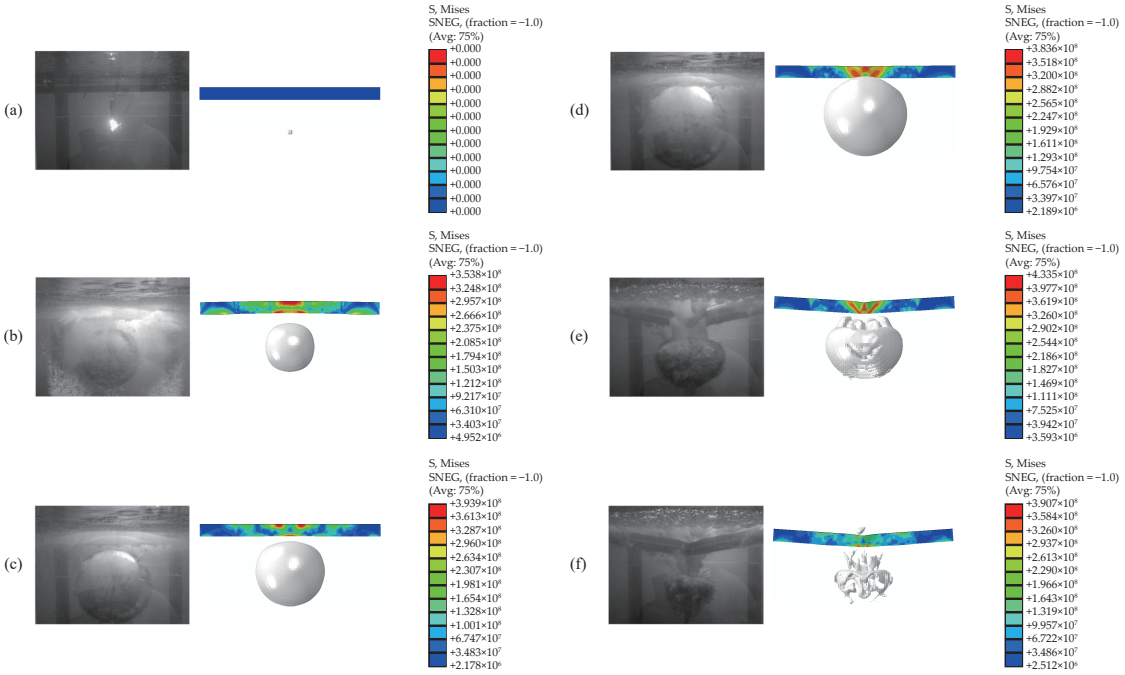


Figure 4. Comparison between experimental photos [23] and calculated cloud pictures: (**a**) 0 ms, (**b**) 5 ms, (**c**) 11 ms, (**d**) 20 ms, (**e**) 45 ms, (**f**) 55 ms.

Figure 5 presents the fold shape of the side plates. The local buckling yield is also well reproduced in the calculation, and the fold direction and crease pattern are consistent with the experimental results.

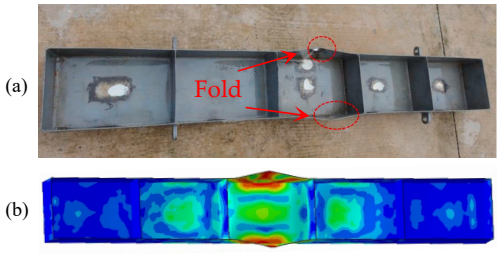


Figure 5. Fold shape of side plates: (**a**) experimental photo [23]; (**b**) calculated cloud picture.

Figure 3 compares the calculated displacement of the SHG middle section with the experimental values. The maximum positive displacement in the experiment was 0.0379 m, and the calculated result was 0.0472 m, with an error of 24.54%. The maximum negative displacement in the experiment was −0.0772 m, and the calculated result was −0.0791 m, with an error of 2.46%. The bubble pulsation period in the experiment was 52.1 ms, and the calculated result was 53.5 ms, with an error of 2.69%. From Figure 3, it can be seen that the variation trend between the experimental results and the calculated results is similar, showing a good correlation. However, the calculated results are larger, which may be because: (1) In the experiment, there are flexible ropes at both ends of the SHG for auxiliary positioning. (2) The CEL method regards the wave velocity as a constant value of the sound speed in the water. However, the closer to the center of the explosive, the greater the impact wave velocity will be, even reaching up to twice the speed of sound in water, which will lead to slower attenuation of the shock wave and a larger overall impulse. (3) The idealization and simplification in the simulation ignore the possible influence of structure manufacturing. In general, the current error is acceptable for the complex and strongly nonlinear problem of near-field underwater explosion damage to ships.

The above comparison shows that the simulation technology and finite element model used can reliably solve the overall and local responses of SHGs subjected to near-field underwater explosion bubbles, which can be used for further work.

4. Results and Analysis

4.1. Bending Mode

As can be seen from the pictures in the validation, when the SHG suffers from sagging damage subjected to the near-field explosion bubble, the two ends move like rigid bodies within a small elastic-plastic limit, and the overall bend is mainly composed of large plastic deformation near the midship, as shown in Figure 6. Moreover, the crease pattern at the bend position has certain regularity. In the process of sagging damage of the SHG, the upper part of the side plates becomes unstable under compression and gradually expands to form several plastic hinge lines. The deformation range of the lower part of the side plates is generally narrower than that of the upper part, specifically shown as W-shaped creases. The deformation of the bottom plate is relatively simple. The plastic hinge lines extend transverse and straight through the whole width. These plastic hinge lines form the overall bend in the SHG. After the plastic hinge lines are formed, the rotation around the yield area becomes easier, and the overall sagging amplitude is often further increased when subjected to bubble collapse force. For the W-shaped creases' local deformation mode on the side plates in this paper, an SHG sagging bend was composed of ten plastic hinge lines, eight on the side plates and two on the bottom plate, as shown in Figure 7.

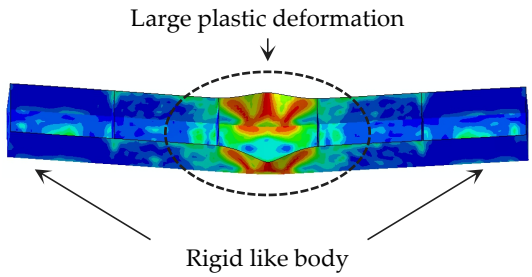


Figure 6. Deformation of sagging damage.

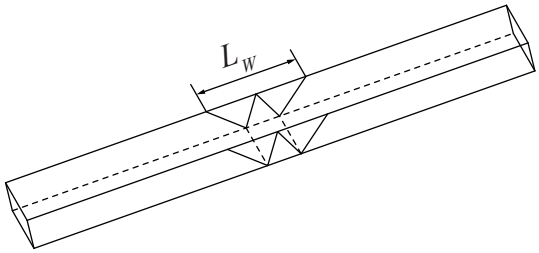


Figure 7. Plastic hinge lines mechanism of W-shaped creases.

As the core deformation damage zone, it is important to predict the length of the potential bend zone when facing a near-field underwater explosion load. Therefore, the length of the bend zone, which is not affected by the transverse bulkhead, is analyzed below. Each part of the hull plate rotates around the plastic hinge lines during the bending process. That is, the bending moment plays a major role. In contrast, the energy dissipated by the expansion and contraction of the hull plates is small; therefore, it is ignored. L_W is used to indicate the length of the bend zone on the undeformed SHG, as shown in Figure 7. M_m represents the average bend moment of the SHG during the bending process. The angle that, at one end, rotates around the middle cross-section is recorded as α. It is assumed that the length of each plastic hinge line on the side plates l has a function related to the length of bend zone L_W and the height of the side plate H; then, the length of different plastic hinge lines can be denoted as $l_i(L_W, H)$. The rotation angle of both sides of each plastic

hinge line is positively related to α, assumed to be $\lambda_i\alpha$. The length of the plastic hinge lines on the bottom plate is the same as the ship width W, and the rotation angle equals α. As the work of external bend moment equals the sum of dissipated energy of the side and bottom plates' plastic hinge lines, we have:

$$2M_m\alpha = 2M_0W\alpha + M_0\alpha\sum_i \lambda_1 l_i(L_W, H), \tag{6}$$

where M_0 is the ultimate bend moment per unit length. According to the principle that the L_W value should make the value of M_m the minimum, let $\partial M_m/\partial L_W = 0$; therefore, we have:

$$\frac{\partial \sum_i l_i(L_W, H)\lambda_i}{\partial L_W} = 0. \tag{7}$$

According to the geometric relations, λ_i is a constant for the determined plastic hinge lines mode. Therefore, L_W has a function that only depends on H. To find the relation between L_W and H, keeping the width of SHG unchanged, the sagging damage responses with height–width ratios of 0.4, 0.5, 0.6 and 0.7, under the same load conditions as Section 3.2, are calculated. The creases are all in a similar W-shaped pattern. The lengths of the bend zones are listed in Table 3 and fitted in Figure 8. The three functions in Figure 8 can fit the relationship between the bend zone's length and the side plates' height. In sum, the correlation coefficient of the formula

$$L_W = 2.43H \tag{8}$$

is closest to 1, and the form is convenient for application; therefore, this linear relation is adopted.

Table 3. Length of SHGs bend zone with different height–width ratios.

Height–Width Ratio	L_W/m
0.4	0.18
0.5	0.24
0.6	0.28
0.7	0.36

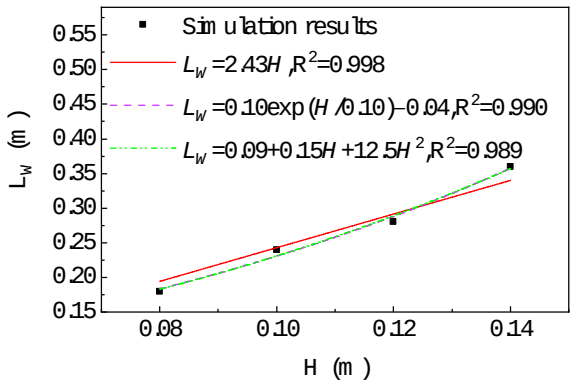


Figure 8. Formula fitting of bend zone length.

The length data of the bend zone can be obtained from the calculation results of the finite element model using the following method. The top edge rotation angle was plot around the z-axis (UR3), the bottom edge rotation angle was plot around the y-axis (UR2), and their differential curves are shown in Figure 9. Points 1-5 are the endpoints of plastic hinge lines. The angle at the crease endpoint changes significantly, that is, the peak points of the differential curve.

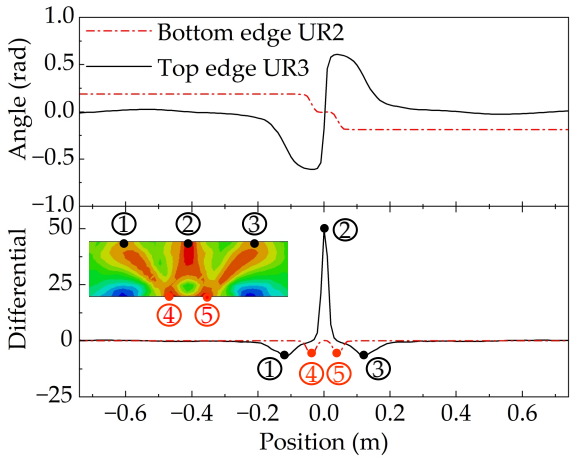


Figure 9. Rotation angle and its differential of side plate's sides.

4.2. Effect of Transverse Bulkheads on Bend Damage

When the transverse bulkheads are located in the potential bend zone, this will obviously have a greater influence on the bend and creases. When the transverse bulkheads are located outside the potential bend zone, this may also have some influence. Therefore, to investigate the transverse bulkhead's effect on the bend damage characteristics of SHGs, the internal structure was redesigned based on the SHG used in the validation. Figure 10 presents the SHG configuration diagram. The origin of the coordinate is located in the center of the bottom plate, and the arrangement of the transverse bulkheads is symmetrical about the yoz coordinate plane. By changing the position, eight kinds of SHGs are designed, as shown in Table 4. The numbering rules are as follows: SHG is the abbreviation of simplified hull girder, and the number in brackets is the dimensionless position of transverse bulkheads x^*. The calculation formula of x^* is:

$$x^* = \frac{2|x|}{L}. \tag{9}$$

For example, SHG(0) indicates that the transverse bulkhead is located at the midsection; SHG(1) indicates that the transverse bulkhead coincides with the end plate, i.e., there is no transverse bulkhead. Through the structural response results of SHGs with the staggered and orderly distribution of transverse bulkheads, the bearing effect of transverse bulkheads can be analyzed to some extent.

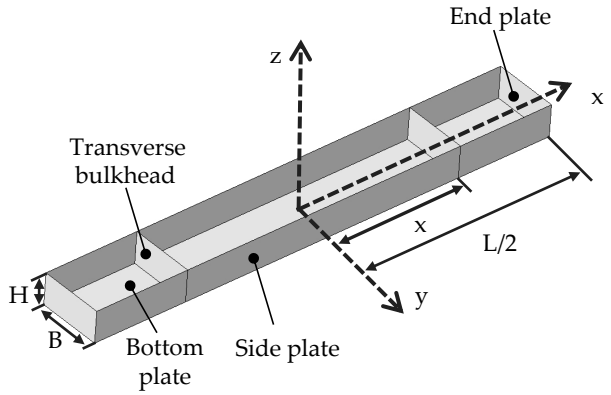


Figure 10. Schematic diagram of SHG.

Table 4. Number of SHGs with different transverse bulkheads.

Nmber	SHG
SHG(0)	
SHG(0.1)	
SHG(0.2)	
SHG(0.33)	
SHG(0.4)	
SHG(0.6)	
SHG(0.8)	
SHG(1)	

To study the bend damage patterns, all SHGs were subjected to the same load conditions as the verification experiment. After checking the results, the unbent SHGs were allowed to bend to a certain extent by keeping the charge unchanged and gradually reducing the detonation distance. The final calculation cases are shown in Table 5.

Table 5. Calculated cases.

Case	Structure	Charge/kg	Detonation Distance/m	SF/($kg^{1/2}$/m)
1	SHG(0)	0.01	0.25	0.180
2	SHG(0.1)	0.01	0.25	0.180
3	SHG(0.2)	0.01	0.25	0.180
4	SHG(0.33)	0.01	0.25	0.180
5	SHG(0.4)	0.01	0.25	0.180
6	SHG(0.6)	0.01	0.25	0.180
7	SHG(0.8)	0.01	0.25	0.180
8	SHG(1)	0.01	0.25	0.180
9	SHG(0.1)	0.01	0.20	0.225
10	SHG(0)	0.01	0.20	0.225
11	SHG(0)	0.01	0.15	0.300

There are several obvious different bend characteristics in the calculation results. These in clude whether the position is central or off-center, whether there are one or two bends, and whether the size is affected by the transverse bulkheads. Figure 11 shows the crease evolution process of the bend position with the following characteristics: (a) size is not affected by the transverse bulkheads and there is a single center bend, (b) size is affected by the transverse bulkheads and there is a single center bend, (c) size is affected by the transverse bulkheads and there is a single off-center bend, and (d) size is affected by the transverse bulkheads and there are double off-center bends.

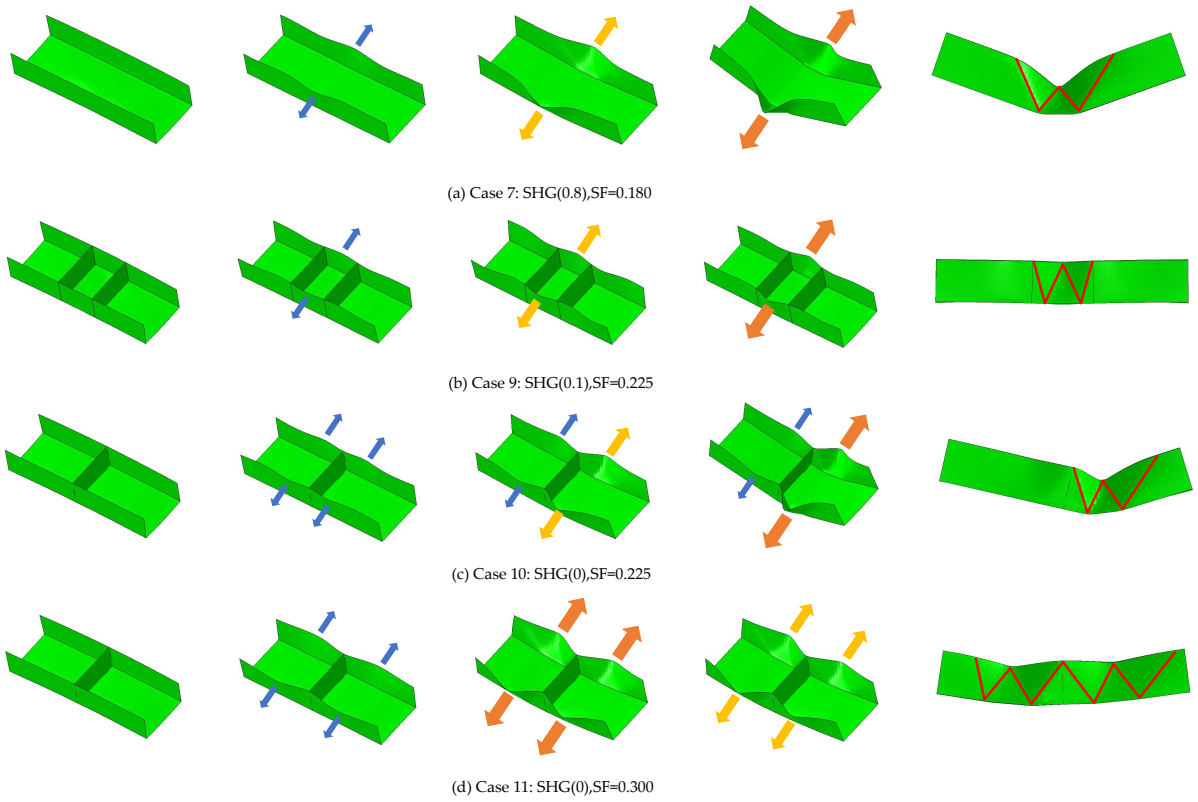


Figure 11. Local creases evolution process: (**a**) 5 ms, (**b**) 13 ms, (**c**) 30 ms, (**d**) 52 ms.

When the transverse bulkheads are located outside the bend zone, it is difficult to effectively limit the crease formation process. The crease expansion is only affected by the hull plates, as shown in Figure 11a. When the transverse bulkheads are located in the bend zone, the creases are limited between the two transverse bulkheads, the space available for side plate deformation becomes small, and the overall bend resistance is effectively improved, as shown in Figure 11b. When the transverse bulkhead is located directly above the explosive, the side plates at the corresponding position are firmly fixed, and it is difficult to produce a transverse deformation. Therefore, it is difficult for the two ends of the SHG to rotate with the transverse bulkhead as the center; therefore, the bend position is offset to both sides of the transverse bulkhead. Depending on the load conditions, there can be one or two bends, as shown in Figure 11c,d. As for Figure 11d, because the explosive is too close to the water surface, the air is sucked in during the bubble contraction, which destroys the internal pressure state, leading to an early recovery time for sagging amplitude. In general, the relative longitudinal position of the explosive and the transverse bulkhead will affect the bend position and size, and the load strength will affect the bend quantity. In the results of this paper, all the side plate creases are W-shaped. However, more crease patterns may appear under different conditions, which requires further study.

Table 6 lists the damage results for SHGs in different cases. The ratio of transverse bulkhead position to half of the bend zone length was used to characterize the parameter of the relative position of the transverse bulkhead and bend zone, i.e., x_W. The calculation formula is

$$x_W = \frac{2|x|}{L_W}. \tag{10}$$

In cases 1 and 2, the SHGs move in whipping mode, so there is no bend zone. The large error in case 3 is due to the influence of the transverse bulkhead, which increases the length of the bend zone by about 12%, indicating that a $1 \leq x_W \leq 1.23$ transverse bulkhead will slightly increase the length of the bend zone. The error in case 9 is large because

the transverse bulkheads are located within the predicted bend zone, which restricts the outward development of plastic hinge lines. The same SHG was used in cases 10 and 11. However, the error in case 10 is larger because the load input energy is smaller than in case 11. Part of the load energy is absorbed by the warping deformation of the left hull plate, resulting in a smaller bend zone length. It can be seen from case 11 that when the load is strong enough, the length of the off-center bend zone with only one constrained side can also be well predicted. It can be seen from cases 4-8 that the transverse bulkheads with $x_W \geq 2.47$ have little influence on the length of the bend zone. Thus, when the bend zone is less affected by the transverse bulkheads, the prediction error of the formula is less than 5%, which can reflect the potential bend zone length and provide a reference for the anti-impact work of ships.

Table 6. Damage results.

Case	x_W	SF/(kg$^{1/2}$/m)	Damage Situation	Simulation Bend Length/m	Error from Formula
1	0	0.180	whipping	-	-
2	0.62	0.180	whipping	-	-
3	1.23	0.180	sagging, center and single bend	0.28	13.2%
4	2.04	0.180	sagging, center and single bend	0.25	2.8%
5	2.47	0.180	sagging, center and single bend	0.24	1.25%
6	3.70	0.180	sagging, center and single bend	0.25	2.8%
7	4.94	0.180	sagging, center and single bend	0.25	2.8%
8	6.17	0.180	sagging, center and single bend	0.24	1.25%
9	0.62	0.225	sagging, center and single bend	0.13	86.9%
10	0	0.225	sagging, off-center and single bend	0.22	10.5%
11	0	0.300	sagging, off-center and double bends	0.25 0.25	2.8% 2.8%

4.3. Effect of Transverse Bulkheads on Overall Bend Strength

To analyze the effect of the transverse bulkhead position on the overall bend strength of SHGs, the overall response results of eight different SHGs under the same load in cases 1–8 are analyzed below. Figure 12 shows the contours of different SHGs at various times. The arrows indicate the direction of motion, and the symbols on the curves indicate the position of transverse bulkheads. At an early stage of the explosion, the middle of the SHGs rapidly displaces under the combined action of a spherical shock wave and bubble expansion boundary. Moreover, the displacement of both ends is relatively slow due to the inertial effect, so the overall structure presents hogging bend deformation, as shown in Figure 12a. In Figure 12b, the main action time of the shock wave has passed. Under the influence of material resilience, the overall deformation gradually enters the unloading stage, and the bend amplitudes decrease to varying degrees. At this moment, the deflection amplitude of all structures is within 0.0025 m, and the ratio to the total length is 1.67‰, so the SHGs can be consideed close to the horizontal state. In Figure 12c, all the structures show a sagging bend, and the deflection amplitude significantly varies among the different structures. After the bubble reaches its maximum volume, it starts to rapidly shrink the boundary. All the structures are driven downward by this, which also causes the sagging bend amplitude of SHG(0.2), SHG(0.33), SHG(0.4), SHG(0.6), SHG(0.8), and SHG(1) to expand further and form sagging damage. However, the deflection amplitude of SHG(0) and SHG(0.1) is not obviously affected, as shown in Figure 12d,e. After the bubble shrinks to the minimum volume, it expands again. The SHGs begin to move upward under the comprehensive action of the expansion bubble boundary, pulsating pressure, jet flow, and restoring force. The sagging amplitudes are restored to different degrees. The deformation of SHG(0) and SHG(0.1) turns into an upward bend, as shown in Figure 12f. The general response mode of SHG(0) and SHG(0.1) is a whipping motion, and the rest of the SHGs appear to undergo different degrees of sagging damage.

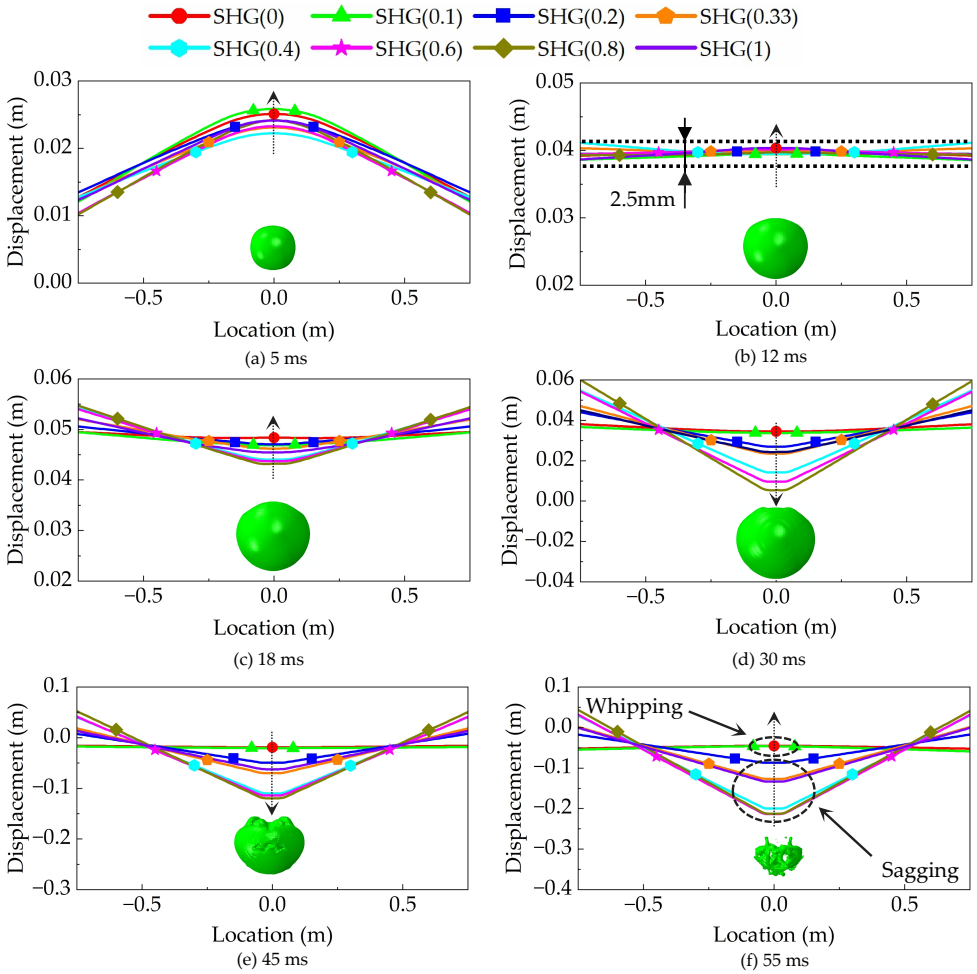


Figure 12. Contours of simplified hull girders: (**a**) 5 ms, (**b**) 12 ms, (**c**) 18 ms, (**d**) 30 ms, (**e**) 45 ms, (**f**) 55 ms.

In summary, the response behavior and damage degree of SHGs with different transverse bulkhead configurations are significantly different under the same load. This shows that transverse bulkheads can contribute important longitudinal strength when facing a near-field underwater explosion load, and the effect of transverse bulkheads differs at different positions. When predicting the overall damage behavior of the structure, attention should be paid to the longitudinal position parameters of different transverse bulkheads.

The dimensionless deflection $w^* = w/L$ is introduced as a parameter to characterize the relative bend degree of SHGs. Figure 13 shows the dimensionless deflection time–history curves of each structure. For these SHGs, if the transverse bulkhead is at the boundary of the predicted bend zone, the corresponding structure number is SHG(0.162). As seen from Figure 13, there are great differences between the deflection of SHGs with transverse bulkhead position parameters greater than 0.162, indicating that the transverse bulkhead outside the bend zone greatly influences the overall damage. In addition, SHGs with different transverse bulkhead configurations show little difference in hogging behavior but a great difference in sagging behavior. This is because, when bent downward, the upper part of the side plate is compressed, and the lower part is stretched. The bend requires yielding and folding in the upper part to make space. Similarly, in the hogging bend, the lower part of the side plates will appear more yielding and folding. For the SHG structure without the deck used in this paper, the lower part of the side plates is orthogonally connected with the bottom plate to form a strong constraint, which is more difficult to yield than the upper part.

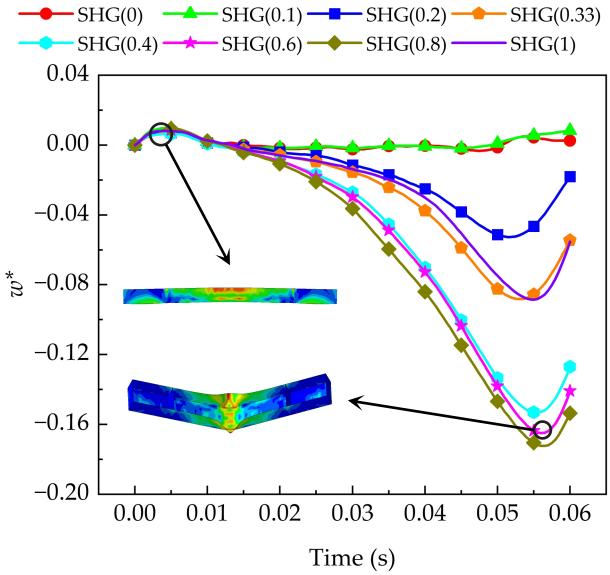


Figure 13. Time history curves of dimensionless deflection.

Further, the maximum sagging amplitudes of each structure are given as statistics in Figure 14. For the SHGs with transverse bulkheads, the response changes from whipping motion to sagging damage as the x^* increases. With the change in position, the restraining ability of the transverse bulkhead to sagging amplitude is shown to have a three-stage pattern, from strong to weak. The transverse bulkhead in the bend zone can significantly reduce the overall bend amplitude. The transverse bulkhead located outside the bend zone also has a non-negligible effect. For example, SHG(0.8) has a 94.5% change in deflection relative to SHG(1) without transverse bulkheads. The sagging deflection of SHG(1) without a transverse bulkhead is between SHG(0.2) and SHG(0.33) and is not the maximum. This indicates that the transverse bulkhead does not always play a positive role in the bearing near-field explosion bubble load. This is because the transverse bulkhead at a far position will reduce the load-sharing capacity of the structure outside the bend zone, causing the load to become more concentrated in the bend zone. The deflection of SHG(0) is slightly greater than that of SHG(0.1). The reason for this is that the bend position of the transverse bulkhead at the mid-section will be offset, and these two have different deformation modes.

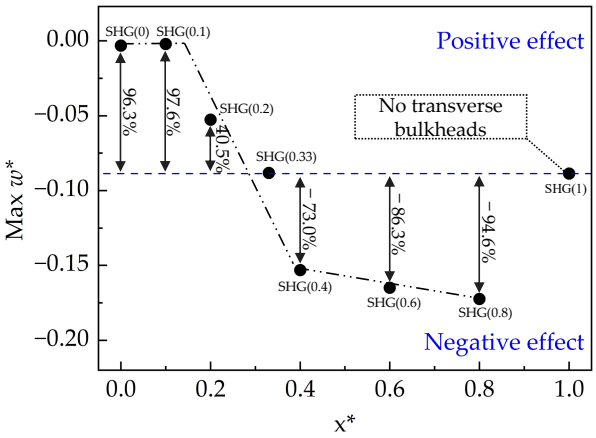


Figure 14. Maximum sagging deflection of different SHGs.

The above results show that the distant transverse bulkhead has a significant influence on the deflection, and it is difficult to properly characterize the overall bend resistance with the parameters of a single section. Therefore, based on the moment of inertia, the equivalent moment of inertia considering the influence of transverse bulkheads at different positions was constructed for evaluation:

$$I_{pe} = I_s + \sum_i \gamma_i I_b, \tag{11}$$

where I_{pe} is the equivalent moment of inertia of SHGs, I_s is the moment of inertia of the SHGs without the transverse bulkhead section, I_b is the moment of inertia of the transverse bulkhead section, and γ_i is the weight coefficient of the transverse bulkhead at different positions. For this paper, I_s = 80.88 cm^4, I_b = 1666.66 cm^4. Assuming that the maximum sagging deflection of SHGs is inversely proportional to the equivalent moment of inertia when the load and ship shape is constant, the weight coefficient function of transverse bulkheads at different positions can be calculated according to Formula (11) and Figure 14, as shown in Figure 15, and the expression is:

$$\gamma = \begin{cases} 1 - 0.0113x^* & 0 < x^* \leq \frac{L_W}{L} \\ 0.0432 - 0.1376x^* & \frac{L_W}{L} < x^* \leq 0.3882 \\ -0.0087 - 0.0039x^* & 0.3882 < x^* < 1 \end{cases}, \tag{12}$$

where L_W/L is the boundary position of the bend zone. It can be seen that, when facing a near-field underwater explosion load, the transverse bulkhead in the bend zone makes a significant positive contribution to the overall bend strength. Therefore, it can be considered to properly strengthen the transverse bulkhead in the potential bend zone in the actual ship, such as using high-strength steel. The transverse bulkhead outside the bend zone may play a positive or negative role. Although the contribution coefficient is relatively small, the influence on the equivalent moment of inertia cannot be ignored due to the large difference between I_s and I_b. It should be noted that the transverse bulkhead weight coefficient function of Equation (12) is mainly for the SHG configuration used in this paper. Different SHGs with more transverse bulkheads will be more complicated and require further study.

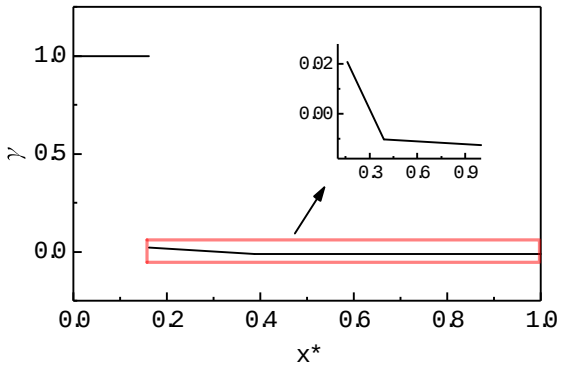


Figure 15. Weight coefficient of transverse bulkhead.

5. Conclusions

To investigate the mechanisms and rules of SHGs' sagging damage when subjected to a near-field underwater explosion bubble, the CEL two-way fluid–structure interaction was adopted, verifying the model's accuracy. Afterward, the responses of 11 SHGs subjected to the near-field underwater explosion were simulated. Then, the plastic hinge lines and size of the bend zone were investigated, and the defensive effect of transverse bulkheads was analyzed. Finally, the equivalent moment of inertia considering distant transverse bulkheads was constructed to evaluate the overall longitudinal bend resistance. The main conclusions can are summarized as follows:

(1) The finite element model of SHG for near water surface and near-field underwater explosion based on the CEL method is verified by comparison with the literature experiment. The calculation results agree with the experimental data and show consistency regarding the crease pattern on the side plates. This indicates that the computing method can be used for further related work.

(2) Regarding sagging damage, the overall bend in the SHGs is composed of multiple plastic hinge lines on the hull plates and mainly depends on the local folding of the side plates. For the bending mode where the creases on side plates are W-shaped, a bend comprises ten plastic hinge lines: eight on the side plates and two on the bottom plates. The transverse bulkhead longitudinal relative position and load strength affect the bend position, size, and quantity.

(3) For the sagging damage of the W-shaped creases, the formula (2.43 times the height of the side plate) for estimating the length of the potential bend zone of the SHGs is given by the regression method. This formula mainly applies to predictions regarding the sagging damage area of the most basic hull plate configuration (opening, no additional structure) subjected to near-field underwater explosions. The error of this formula is less than 5% for cases in this paper, which can provide a reference for the anti-impact work of ships. In practice, the creases are not sharp but have a certain curvature, which will expand the core deformation zone. Therefore, it is recommended to multiply the appropriate safety factor when using the formula for estimation.

(4) When facing the near-field underwater explosion load, the transverse bulkhead, not only on the corresponding section but also at a certain distance, has an important influence on the total longitudinal strength. When located in the bend zone, the transverse bulkheads can enhance the overall bend resistance by increasing the local strength and limiting the development of creases on the side plates. On the other hand, when located outside the bend zone, the transverse bulkhead has a non-negligible influence, affecting the deflection results in this paper by 94.6%. However, this does not always play a positive role.

(5) The equivalent moment of inertia is established, and the weight coefficient functions of transverse bulkheads at different positions are preliminarily given. The equivalent moment of inertia can appropriately reflect the influence of transverse bulkheads at different positions on the overall bend resistance when the near-field underwater explosion bubble causes sagging damage. The establishment of the weight coefficient is based on the SHG results in the paper, and its applicability to different ship types requires further investigation.

It should be noted that the "W" plastic hinge lines mode that was constructed and the prediction formula are mainly based on an open box hull girder structure used in this paper, which is a foundation form. Evolutionary modes of "W" or other modes may occur when there are additional structures, but the potential bend zone length should be less than the W-shaped zone.

Author Contributions: Conceptualization, W.Z. and Z.D.; data curation, Y.G. and Y.Z.; formal analysis, Y.G.; investigation, Y.G. and W.Z.; methodology, Y.G. and W.Z.; project administration, W.Z. and Z.D.; resources, W.Z.; software, Y.G.; supervision, W.Z. and Z.D.; validation, Y.G. and Y.Z.; visualization, Y.G. and Y.Z.; writing—original draft, Y.G.; writing—review and editing, W.Z. and Z.D. All authors have read and agreed to the published version of the manuscript.

Funding: This research received no external funding.

Institutional Review Board Statement: Not applicable.

Informed Consent Statement: Not applicable.

Data Availability Statement: Not applicable.

Conflicts of Interest: The authors declare no conflict of interest.

Abbreviation

The following abbreviations are used in this manuscript:

SHG Simplified hull girder

References

1. Kiciński, R.; Szturomski, B. pressure wave caused by trinitrotoluene (TNT) underwater explosion—Short review. *Appl. Sci.* **2020**, *10*, 3433. [CrossRef]
2. Helal, M.; Huang, H.; Fathallah, E.; Wang, D.; Mokbel ElShafey, M.; Ali, M.A. Numerical Analysis and Dynamic Response of Optimized Composite Cross Elliptical Pressure Hull Subject to Non-Contact Underwater Blast Loading. *Appl. Sci.* **2019**, *9*, 3489. [CrossRef]
3. Cao, L.; Fei, W.; Grosshans, H.; Cao, N. Simulation of underwater explosions initiated by high-pressure gas bubbles of various initial shapes. *Appl. Sci.* **2017**, *7*, 880. [CrossRef]
4. Zamyshlyaev, B.V.; Yakovlev, Y.S. *Dynamic Loads in Underwater Explosion*; Technical Report; Naval Intelligence Support Center: Washington, DC, USA, 1973.
5. Vernon, T.A. *Whipping Response of Ship Hulls from Underwater Explosion Bubble Loading*; Technical Report; Defence Research Establishment Atlantic Dartmouth: Dartmouth, NS, Canada 1986.
6. Geers, T.L.; Hunter, K.S. An integrated wave-effects model for an underwater explosion bubble. *J. Acoust. Soc. Am.* **2002**, *111*, 1584–1601. [CrossRef] [PubMed]
7. Ma, W.; Zhao, X.; Gilbert, C.; Wang, K. Computational analysis of bubble–structure interactions in near-field underwater explosion. *Int. J. Solids Struct.* **2022**, *242*, 111527. [CrossRef]
8. Gannon, L. Simulation of underwater explosions in close-proximity to a submerged cylinder and a free-surface or rigid boundary. *J. Fluids Struct.* **2019**, *87*, 189–205. [CrossRef]
9. Javier, C.; Galuska, M.; Papa, M.; LeBlanc, J.; Matos, H.; Shukla, A. Underwater explosive bubble interaction with an adjacent submerged structure. *J. Fluids Struct.* **2021**, *100*, 103189. [CrossRef]
10. Ramajeyathilagam, K.; Vendhan, C.P. Deformation and rupture of thin rectangular plates subjected to underwater shock. *Int. J. Impact Eng.* **2004**, *30*, 699–719. [CrossRef]
11. Chung Kim Yuen, S.; Nurick, G.N. Experimental and numerical studies on the response of quadrangular stiffened plates. Part I: Subjected to uniform blast load. *Int. J. Impact Eng.* **2005**, *31*, 55–83. [CrossRef]
12. Suresh, C.; Ramajeyathilagam, K. Large deformation behaviour of thin mild steel rectangular plates subjected to underwater explosion loading under air and water backed conditions. *Appl. Ocean. Res.* **2021**, *114*, 102780. [CrossRef]
13. Schiffer, A.; Tagarielli, V.L. One-dimensional response of sandwich plates to underwater blast: Fluid-structure interaction experiments and simulations. *Int. J. Impact Eng.* **2014**, *71*, 34–49. [CrossRef]
14. Zhang, Z.; Jin, X. Study on the energy dissipation mechanism of the pyramidal lattice sandwich panel subjected to underwater explosion. *Mar. Struct.* **2022**, *85*, 103243. [CrossRef]
15. Gargano, A.; Das, R.; Mouritz, A.P. Comparative experimental study into the explosive blast response of sandwich structures used in naval ships. *Compos. Commun.* **2022**, *30*, 101072. [CrossRef]
16. Mohotti, D.; Fernando, P.L.N.; Weerasinghe, D.; Remennikov, A. Evaluation of effectiveness of polymer coatings in reducing blast-induced deformation of steel plates. *Def. Technol.* **2021**, *17*, 1895–1904. [CrossRef]
17. Liu, J.; An, F.J.; Wu, C.; Liao, S.S.; Zhou, M.X.; Xue, D.Y.; Guo, H. Experimental investigations on small-and full-scale ship models with polyurea coatings subjected to underwater explosion. *Def. Technol.* **2021**, *18*, 1257–1268. [CrossRef]
18. Zhang, Z.H.; Wang, Y.X.; Zhao, H.F.; Qian, H.F.; Mou, J.L. An experimental study on the dynamic response of a hull girder subjected to near field underwater explosion. *Mar. Struct.* **2015**, *44*, 43–60. [CrossRef]
19. Li, H.T.; Zheng, X.Y.; Zhang, C.; Mei, Z.Y.; Bai, X.F.; Liu, K. Sagging damage characteristics of hull girder with trapezoidal cross-section subjected to near-field underwater explosion. *Def. Technol.* **2021**. [CrossRef]
20. Li, H.T.; Zhang, C.; Zheng, X.Y.; Mei, Z.Y.; Bai, X.F. A simplified theoretical model of the whipping response of a hull girder subjected to underwater explosion considering the damping effect. *Ocean. Eng.* **2021**, *239*, 109831. [CrossRef]
21. Wang, J.X.; Zong, Z.; Liu, K.; Cui, J. Simulations of the dynamics and interaction between a floating structure and a near-field explosion bubble. *Appl. Ocean. Res.* **2018**, *78*, 50–60. [CrossRef]
22. Gan, N.; Yao, X.L.; Liu, L.T.; Xiao, W.; Wang, X.L. Research on overall damage characteristics of a hull girder under explosion bubble collapse. *Ocean. Eng.* **2019**, *188*, 106315. [CrossRef]
23. Gan, N.; Liu, L.T.; Yao, X.L.; Wang, J.X.; Wu, W.B. Experimental and numerical investigation on the dynamic response of a simplified open floating slender structure subjected to underwater explosion bubble. *Ocean. Eng.* **2021**, *219*, 108308. [CrossRef]
24. Benson, D.J.; Okazawa, S. Contact in a multi-material Eulerian finite element formulation. *Comput. Methods Appl. Mech. Eng.* **2004**, *193*, 4277–4298. [CrossRef]
25. Simulia, D. Abaqus 6.11 Analysis User's Manual. Abaqus 6.11 Documentation. 2011; Volume 25, pp. 568–584. Available online: http://130.149.89.49:2080/v6.11/books/usb/default.htm (accessed on 1 February 2023).

Disclaimer/Publisher's Note: The statements, opinions and data contained in all publications are solely those of the individual author(s) and contributor(s) and not of MDPI and/or the editor(s). MDPI and/or the editor(s) disclaim responsibility for any injury to people or property resulting from any ideas, methods, instructions or products referred to in the content.